Increasing the speed of an InP-based integration platform by introducing high speed electro-absorption modulators

Increasing the speed of an InP-based integration platform by introducing high speed electro-absorption modulators

Marija Trajkovic, *Student Member, IEEE,* Fabrice Blache, Helene Debregeas, Kevin A. Williams, and Xaveer J. M. Leijtens, *Senior Member, IEEE*

***Abstract*—We report high speed electro-absorption modulators (EAMs), designed, fabricated and characterized within an open access generic foundry process. The EAM as a new building block (BB) is optimized in the existing platform, in which other BBs are established. By optimizing the EAM design layout, we show a static extinction ratio (static ER) of 18 dB, a low DC bias voltage below 1 V at increased temperature, as well as operation in a semi-cooled environment, tested in the range of 20–60ºC. Furthermore, we improve the intrinsic S-parameter response with a co-design circuit. The intrinsic 3-dB bandwidth of a 100 µm-long EAM is 17 GHz. When measured with the EAM submount design, it is increased to 24 GHz. Simultaneously, the return loss bandwidth is improved by a factor of 2.5 staying below -10 dB up to 20 GHz. Through the realization of the EAM submount design we achieve a three time speed increase of the existing platform, from previously offered 9 GHz (using an electro-optical modulator) to 24 GHz shown in this work.**

***Index Terms*—photonic integrated circuits, electro-absorption modulators, high speed integrated circuits**

I. Introduction

COMMUNICATION demands have been pushing the progress of photonic integrated circuit (PIC) technology requiring higher speed and lower energy for system-on-chip designs [1]. The solution for telecommunication's ever increasing demand for capacity can be found in 1) higher bandwidth per channel [2], 2) higher number of channels [3], and 3) using increasingly complex modulation formats [4] [5]. Wavelength division multiplexing (WDM) is a common technique of combining many channels on a single chip. The increase in total chip capacity requires the integration of many active (laser, modulator, amplifier) and passive components (coupler, arrayed waveguide grating, multimode interferometer, etc.) on a single chip. Open access foundry enabled PICs have demonstrated an aggregate capacity of 300 Gbps [6] [7]. Small building block footprint is preferred when it comes to densely packed PICs. For high speed operation an electro-absorption modulator fulfills the requirement. State-of-the-art EAMs have a separately grown layer stack for a minimal insertion loss using a butt-joint or selective area growth technique [8], a high number of quantum wells (QWs) for high extinction ratio [9], quantum wells based on aluminum quaternaries (InGaAlAs rather than InGaAsP) for a steep extinction ratio curve and reduced saturation effects [10], and a thick dielectric for improved high-frequency performance. Nevertheless, in order to integrate it in a generic photonic platform, certain compromises need to be made. The challenge lies in introducing a new component while keeping the same or improving the platform performance. Using the InP-based active-passive generic integration platform of TU Eindhoven and Smart Photonics [11] [12] we focus on increasing the speed of the current platform by introducing an electro-absorption modulator as a new building block

The existing epitaxial layers [12] offered in the open access multi-project wafer run [13] are used for the EAM building block. Its integration with a widely tunable laser, comprising of semiconductor optical amplifiers, multimode interferometers, phase shifters and passives, has been demonstrated inside the platform [14]. Different methods of the EAM submount designs are described in [15], investigating different options for the electrical circuit design. The EAM dynamic characterization has been reported in [16], demonstrating 32 Gbps error-floor free transmission up to 4 km (maximum bit-rate limited by the measurement equipment).

A detailed design of the new building block for high speed operation is presented in Section II. The characterization of its static parameters, such as static extinction ratio, EAM on-state insertion loss and DC bias voltage are described in Section III.

The temperature variation effects are typically mitigated by a thermo-electric cooler (TEC), however this not only increases power consumption, but also the packaging cost. A modulator which can operate in a wide temperature range is advantageous

This work was supported in part by the European Commission through the Marie Curie GeTPICs project, funded under FP7-PEOPLE under grant agreement no 317316, and STW project Next Generation Foundry Process Development under the grant agreement no 10019120.

Marija Trajkovic (e-mail: m.trajkovic@tue.nl), Kevin A. Williams and Xaveer J. M. Leijtens are with the Institute for Photonic Integration, Eindhoven University of Technology, 5600 MB Eindhoven, the Netherlands.

Fabrice Blache is with III-V Lab, a joint laboratory between NOKIA Bell Labs, Thales Research and Technology, and CEA Leti, Campus de Polytechnique, 1 avenue Augustin Fresnel, 91767 Palaiseau-Cedex, France.

Helene Debregeas is with Almae Technologies, Route de Nozay, 91460 Marcoussis, France.

as it will decrease the overall power consumption. Therefore, we look at the modulator's performance in a semi-cooled environment.

The chirp parameter is measured and described in Section IV. In transmission through a standard single mode fiber (SSMF) dispersion at 1.55 µm broadens the signal. A negative chirp value is desirable as it can compensate for SSMF dispersion, and therefore extend the reach.

Section V describes the EAM submount design, and the extraction procedure of modulator electrical parameters for 3-dB bandwidth optimization. The described submount design creates a resonant peaking in the recorded electro-optical response, improving the overall bandwidth.

Section VI summarizes a trade-off between the static extinction ratio and electro-optical bandwidth, for optimized modulator performance.

II. Building Block Design

The current InP generic integration platform is based on an n–doped substrate, where the epitaxial growth of active and passive sections is integrated using a butt-joint technique. The existing layer stack for amplifiers/lasers, centered around 1.55 µm, is used for the modulator structure as well. When reversely biasing the EAM, absorption changes with the applied electric field, known as the quantum-confined Stark effect (QCSE). The p-i-n layers are designed to form a deeply etched ridge waveguide with a nominal width w = 1.5 µm, and a typical thickness of the intrinsic region d ~ 500 nm. The top metal is placed on top of a dielectric, in order to reduce modulator access pad capacitance, discussed in detail in Section V. Its footprint should be as small as possible and is limited by the requirements for the wire-bonding. Fig. 1 shows a top view photograph of the fabricated EAM chip integrated with passive waveguides. The chip width is 1.5 mm and its length is 4 mm. Anti-reflection (AR) coatings are applied on both sides of the chip to suppress the reflection loss and avoid multiple optical paths in the modulator section. Short isolation sections next to the MQW region are included for electrical isolation. The access pads are designed in a ground-signal-ground (GSG) configuration, where the ground is placed on n-InP for access to the top n-contact.

III. Static Parameter Characterization

The total insertion loss is defined as the ratio of the output over the input light intensity, and gives information about the total losses in the system as a function of the applied DC bias voltage. The ratio of the output power at different bias points and at V = 0 V gives the static extinction ratio. The static ER

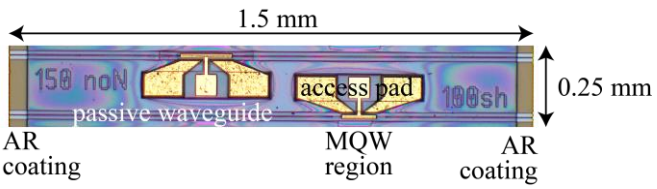

Fig. 1. Top view of the fabricated EAM chip with two modulators.

depends on the QW absorption $\Delta\alpha$ determined by the material properties, the confinement factor Γ of the optical mode inside the QWs, and the length of the modulator section L. Using the existing epitaxial structure in the generic photonic platform, we vary the length of the EAM from 50–250 µm.

A. Experimental setup

An external widely tunable laser source (1490–1610 nm) was used to inject light into the modulator section, setting the laser output power to 0 dBm. At the input of the EAM a polarization maintaining lensed fiber is edge-coupled and aligned to the TE orientation, as the QCSE-induced absorption is polarization dependent. The output chip power is recorded with a power meter. The fiber coupling lead to ~4 dB coupling loss at each facet. The transmission loss in the passive waveguides integrated with the EAM is 0.23 dB for 1.4 mm waveguide length, consistent with foundry expectations. The measurements are carried out at room-temperature without temperature stabilization, except for the temperature dependence measurement.

B. Static extinction ratio and on-state insertion loss

The static ER is found from the wavelength dependent transmission response, shown in Fig. 2a. We record the output optical power dependence on the applied voltage ranging from 0 to -6 V with a step of 0.1 V. The measurement includes coupling and transmission loss. The wavelength dependence of the static ER depends on the device structure (w, L) and on the operating conditions: the detuning ($\Delta\lambda$) between the modulator bandgap and the operating laser wavelength. The EAM bandgap is set at 1.55 µm, hence it operates in the L-band. For

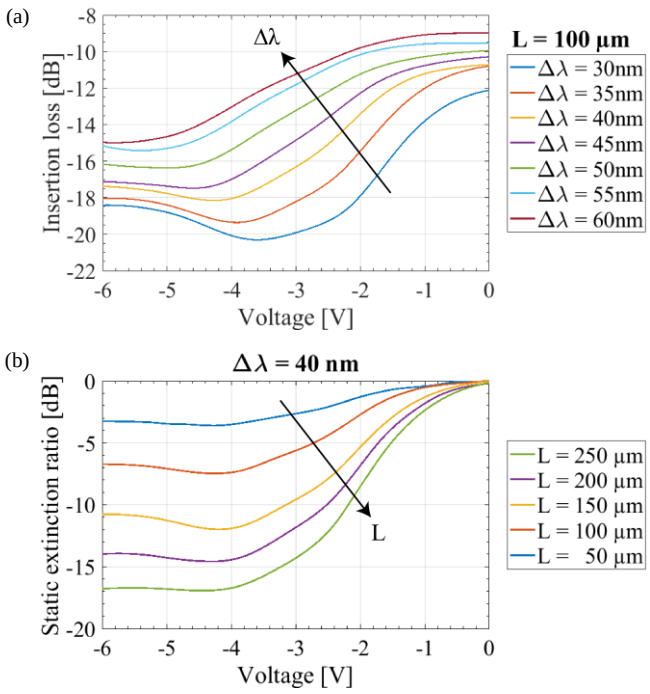

Fig. 2. The recorded output power as a function of the reverse DC bias for (a) a different detuning and 100 µm-long EAM, and (b) a different modulator length at 40 nm fixed detuning.

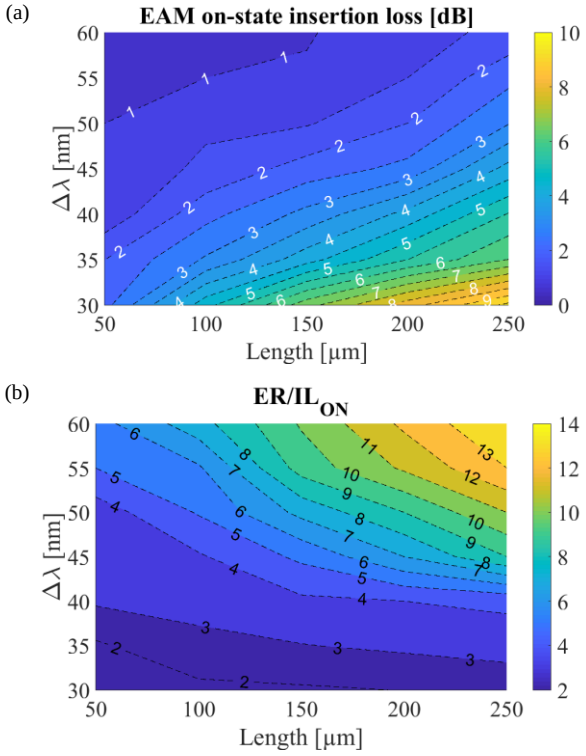

Fig. 3. (a) Measured on-state insertion loss depending on the detuning from the incident light and the EAM length. The values are in the range of 0.5–9 dB. (b) The static ER over IL_{ON} for various detuning and EAM length.

a dense WDM operation in the C-band, the bandgap could be changed to lower values, around 1.5 μm, with no significant influence on the performance.

Fig. 2a shows that a large detuning of 60 nm reduces the insertion loss, but degrades the static extinction ratio. Therefore, a higher reverse bias is needed to achieve the same operating condition. For lower detuning the exciton peak is more pronounced, which is visible for detuning below 45 nm. Fig. 2b shows the static extinction ratio for different EAM lengths at 40 nm detuning. For 50–250 μm modulator length we obtain 4–18 dB static ER, respectively.

Together with the static ER the on-state insertion loss (IL_{ON}) needs to be determined. The on-state insertion loss represent the losses inside the active section at V = 0 V. Fig. 3a shows IL_{ON} change with the detuning and the EAM length. A longer modulator gives a larger ER, but also a larger IL_{ON}. Therefore, a trade-off exists between the static ER and the on-state insertion loss. For this reason, a figure of merit ER/IL_{ON} is introduced and shown in Fig. 3b. A detuning of 30 nm results in a figure of merit of ~2, while a 60 nm detuning for a 250 μm-long EAM gives a figure of merit of 14.

C. Optimal DC bias voltage

Determining the required DC bias voltage is important for the driving electronics. In practice, the smaller the value the better for the electronic circuit. The optimal DC bias point is found from the minimum of the transfer curve first derivative, i.e. inflexion point, shown in Fig. 4. A difference in detuning

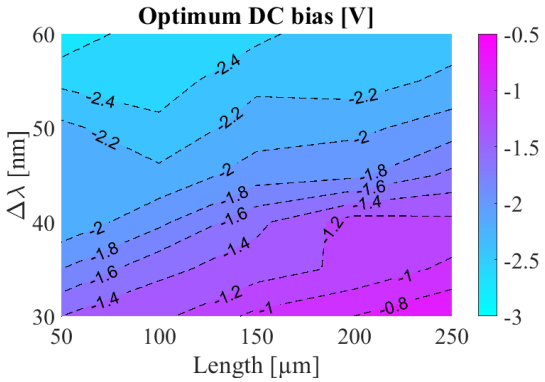

Fig. 4. The optimal DC bias voltage depending on the detuning and the modulator length.

from $\Delta\lambda$ = 60 nm to $\Delta\lambda$ = 30 nm cuts the required DC bias voltage in half, from -3 V to -1.5 V.

For a low-voltage operation both a small detuning and a long modulator section are required. However, the figure of merit ER/IL_{ON} has its maxima for a higher detuning, see Fig. 3b. Therefore, another compromise between the optimal DC bias point and the ratio of ER/IL_{ON} exists, depending on the system requirements. For a DC bias operation above -2 V, the factor ER/IL_{ON} can be maximized to 14 and the optical amplification in the system is lowered. On the other side, for DC bias voltage minimization, optical amplification is needed reducing the figure of merit ER/IL_{ON}.

D. Temperature dependence

The choice of the applied DC bias voltage becomes more challenging in a temperature varying environment. The

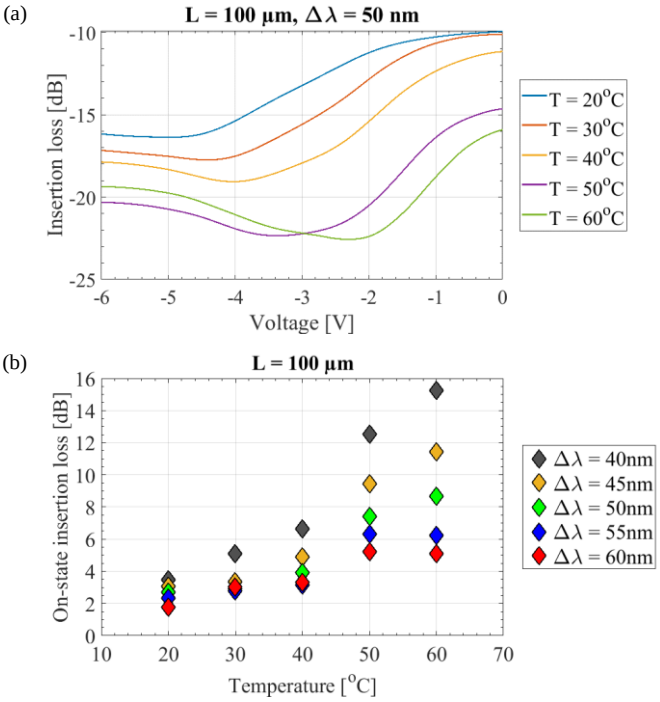

Fig. 5 (a) Transmission curve temperature dependence for 100 μm-long EAM at 50 nm detuning. (b) Temperature influence on the on-state insertion loss for 100μm-long EAM and various detuning.

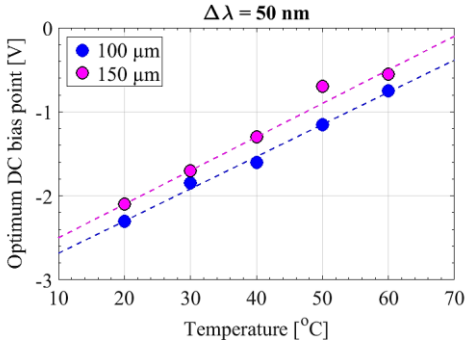

Fig. 6. Optimum DC bias as a function of temperature for two different modulator lengths.

modulator temperature dependence is tested by temperature control of the copper chuck on top of which the chip is positioned. The shift of the transmission curve is presented in Fig. 5a for a semi-cooled operation (20–60ºC). The static ER over the whole measured temperature range stays constant at ~7 dB for the 100 µm-long EAM. A higher temperature change will shift the absorption peak to lower energies, thereby modifying the transmission curve. As the temperature increase has a similar impact on the detuning reduction, we observe a higher on-state insertion loss, but a significant gain in the optimal DC bias voltage, following the inflexion point in Fig. 5a. A summary of the on-state insertion loss values is presented in Fig. 5b. Even for detuning above 50 nm IL_{ON} stays below 9 dB in the whole measured temperature range.

The reduction of the optimal DC bias voltage is observed for the reference 100 µm-long EAM, where the inflexion point at 60ºC is at -0.75 V, as opposed to -2.3 V at room temperature and 50 nm detuning, depicted in Fig. 6. The minimization in required DC bias voltage is in this case achieved at the cost of a higher insertion loss. At moving to even higher temperatures would further reduce the DC bias voltage, at the expense of an increased insertion loss.

IV. Chirp Parameter

According to the Kramers-Kronig relations, a variation of the imaginary part of the dielectric constant (the absorption) results in a variation of its real part introducing a phase modulation, also known as chirp. This effect can be approximated by the chirp parameter α_H:

$$\alpha_H = \frac{\Delta n_r}{\Delta n_i} = \frac{4\pi}{\lambda_0}\frac{\Delta n_r}{\Delta \alpha} \quad (1)$$

where Δn_r is the real part refractive index change, and $\Delta\alpha$ is the absorption change. From Eq. 1 the chirp depends largely on the material properties and the detuning wavelength. A combination of the applied DC bias voltage and the detuning is a practical solution for making the chirp parameter more negative for SSMF dispersion compensation.

A. Characterization setup and results

The measurement technique used to determine the chirp parameter is described in [17]. The method to detect a phase modulation with an external tunable Mach-Zehnder interferometer (MZI), and eliminate the amplitude modulation is shown schematically in Fig. 7a. At two points, A and B, the transfer function (H) is linear, and the measurement at these two points allows for the amplitude modulation elimination. The resulting photocurrent in the photodetector is proportional to the phase variations of the optical signal.

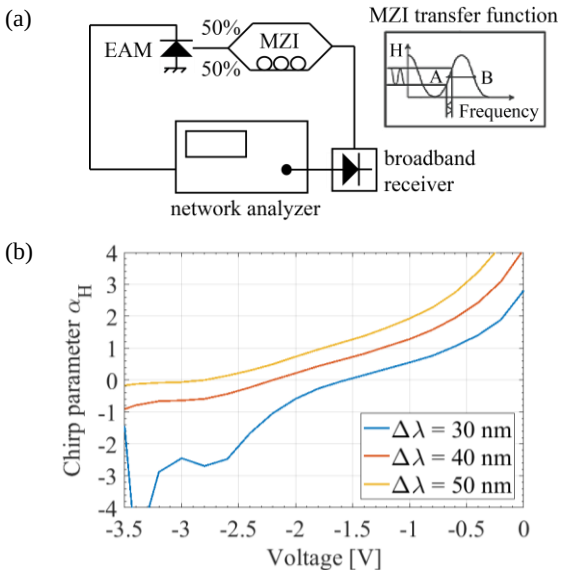

Fig. 7. (a) The measurement setup for the chirp characterization. (b) Chirp as a function of the applied DC bias voltage and for different detuning.

The measured chirp parameter versus the applied DC bias voltage is presented in Fig. 7b, at different detuning wavelengths. The point of interest for the chirp parameter is zero-crossing and its negative values. However, this happens for V >2.2 V at 40 nm detuning. With the on-off keying (OOK) modulation, the chirp will play an important role, as it will change from positive to negative when the drive voltage swing changes from 0 to -4 V.

V. Electronic-Photonic Co-Design

The electronic-photonic co-design is the key for a bandwidth improvement and the electrical signal integrity preservation. The parasitic reactance and the impedance mismatch, originating from interconnects between the electronic and photonic ICs, can degrade the modulating waveform due to reflections and overshoot. The optical modulation and the reflected RF electrical signal are compared to the input RF electrical signal to determine the electro-optical (E/O) transmission (S_{21}) and reflection (S_{11}) coefficient, i.e. the scattering (S) parameters of the device.

The method developed in [18] allows to directly extract the parameters of the access pad, shown in Fig. 8, from its *open* and *short* circuit. The methodology considers that all the parameters are frequency independent. The device bandwidth is defined as the frequency range over which the magnitude of the S_{21} response remains within 3 dB with respect to the S_{21} value at f = 0. Representing the EAM as a lumped RC-network element, and considering its resistance is negligible compared to the source R_s and load impedance R_L, shown in Fig. 8c, the EAM bandwidth is given by:

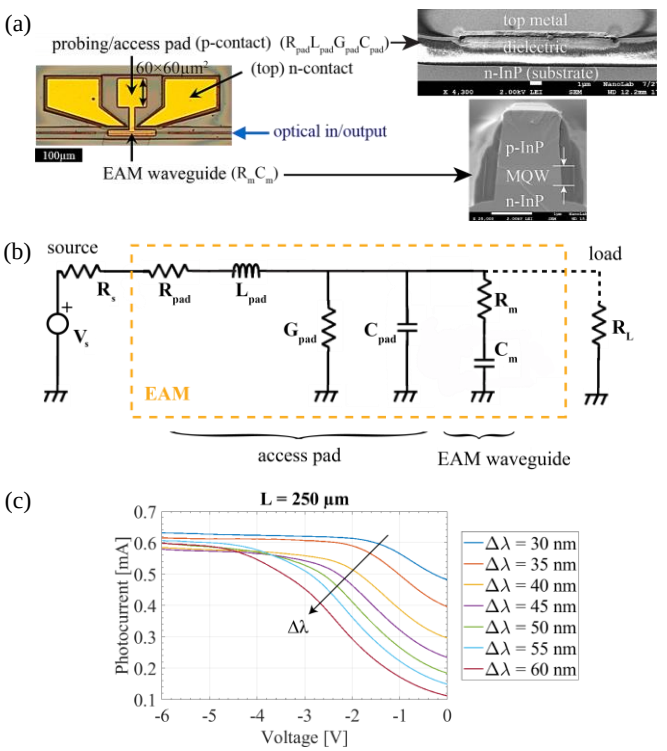

Fig. 8. (a) Top view of the fabricated 100μm-long EAM, and an SEM photo of the access pad and the EAM cross section. (b) Small signal equivalent electrical circuit of the EAM and the access pad with a source impedance *R*s and the load impedance R_L. (c) Bright I-V curve for 250 μm-long EAM and various detuning wavelengths.

$$f_{3dB} = \frac{1}{2\pi\left(\frac{1}{R_S+R_L}\right)^{-1}(C_m+C_{pad})} \qquad (2)$$

where the EAM resistance R_m includes p-InP, and the capacitance C_m represents the depletion of intrinsic i-InP region. From Eq. 2 the reduction of the total capacitance leads to a bandwidth increase. As the EAM capacitance can be represented with a parallel plate approximation, increasing i-InP thickness and decreasing component dimensions will lead to the C_m decrease. However, the increase of i-InP thickness leads to a field strength decrease inside the quantum wells. The model does not include the generated photocurrent, as its value stays below 0.65 mA for the longest measured EAM, shown in Fig. 8d.

A. *Equivalent electrical circuit*

The S_{11}-parameter of the EAM device is measured using Agilent 67 GHz Vector Network Analyzer (N5227A PNA), probing the EAM directly on-chip. A DC bias voltage is set to-2 V for the model extraction, taken from the static parameter optimization. The extraction and optimization process are done in ADS [19] matching the real and imaginary part of the measured and modelled Y and Z-parameters. The access pad is represented as a lossy RLGC-network element (Table 1). R_{pad} and G_{pad} represent the lossy part of the access pad, electrical and dielectric loss, respectively. The conductance value G_{pad} is very low and can be neglected.

The access pad capacitance C_{pad} will influence the overall available bandwidth, therefore its reduction is critical. Placing it on top of a thick polyimide layer (value range in the platform 0.3–2 μm) results in a calculated value of C_{pad} = 64 fF for the best case of 2 μm dielectric height. For n–substrate, a thicker dielectric layer could further decrease the pad capacitance.

R_{pad} (Ω)	L_{pad} (nH)	G_{pad} (mS)	C_{pad} (fF)
1.5	0.003	0.03	103

Table 1. Extracted RLGC parameters of the access pad.

De-embedding the access pad from the total measured EAM structure gives the EAM equivalent electrical circuit's parameters, shown in Table 2. The Table compares the modelled and measured 3-dB bandwidth of the intrinsic and loaded (50 Ω) EAM.

L (μm)	R_m (Ω)	C_m (fF)	$f_{3dB\_int\_model}$ (GHz)	$f_{3dB\_int\_meas}$ (GHz)	$f_{3dB\_50Ω\_meas}$ (GHz)
50	11.3	63	19.2	22	45
100	5.3	134	13.4	17.4	28.5
150	4.8	180	11.2	13.4	23.4
200	4.9	323	7.5	8	17.4
250	4.1	391	6.4	7.6	13.6

Table 2. The extracted EAM parameters, and comparison of 3-dB bandwidth from the model and measured (intrinsic-load free and with 50 Ω parallel termination load inside the RF probe).

B. *3-dB bandwidth*

A commercial O/E calibration module (70 GHz bandwidth photodetector) was added for the electro-optical bandwidth measurement. The intrinsic (load-free) measured and calculated

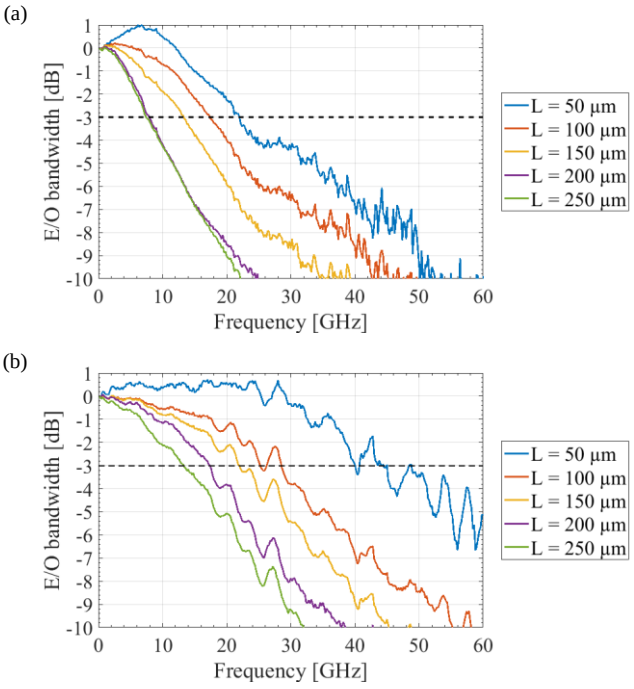

Fig. 9. Measured E/O 3-dB bandwidth of the (a) intrinsic electro-absorption modulator (b) tested with a 50 Ω parallel resistor inside the high-frequency probe.

3-dB modulator bandwidth are summarized in Table 2. The calculated values are estimated from the extracted RC-model.

The EAM impedance is lower than the source impedance of 50 Ω, causing a mismatch and creating reflections. To suppress the back reflection to the driver, the same measurement was repeated with an RF probe, which has a 50 Ω parallel termination load integrated inside it.

The measured E/O response is shown in Fig. 9. Intrinsic (load-free) bandwidth of the EAM is presented in Fig. 9a, whereas Fig. 9b shows the measurement with the 50 Ω parallel termination in the RF probe, improving the frequency response about a factor of two. For lengths ranging from 250 to 50 µm, load-free EAM provides 5–25 GHz bandwidth, and 14–45 GHz with parallel 50 Ω termination load. An excellent match is achieved between measured and calculated values, seen in Table 2, which validates the accuracy of the model.

C. *EAM submount design*

The EAM submount design is made to improve both the E/O bandwidth and the reflection parameter. All the elements are mounted on the CuW carrier platform (Fig. 10a). At the input a grounded-coplanar-waveguide (GCPW) transmission line is designed on alumina (Al_2O_3) to have a characteristic impedance of 50 Ω and keep the signal integrity at the modulator input. The GCPW line and the EAM are connected with a gold wire wedge bond. A 50 Ω termination load is placed after the EAM chip. The power absorbed in 50 Ω termination load has a strong impact on the thermal properties of the module. A broadband decoupling capacitance is placed before the load to avoid the DC power dissipation in the termination load.

The combination of inductive elements (wire bonds ~100 nH) at the input and the output of the modulator, and the EAM junction capacitance create a peaking in the E/O response. The intrinsic E/O bandwidth of the EAM is improved with the EAM submount compared to the load-free case (Fig. 10c). An improvement of 7 GHz is obtained, approaching the value of 28 GHz measured with 50 Ω termination inside the RF probe. The frequency range in which the reflection coefficient stays below -10 dB is increased with the EAM submount design to 20 GHz, seen in Fig. 10b. An improvement by a factor of 2.5 compared to the 50 Ω parallel load in the RF probe is achieved.

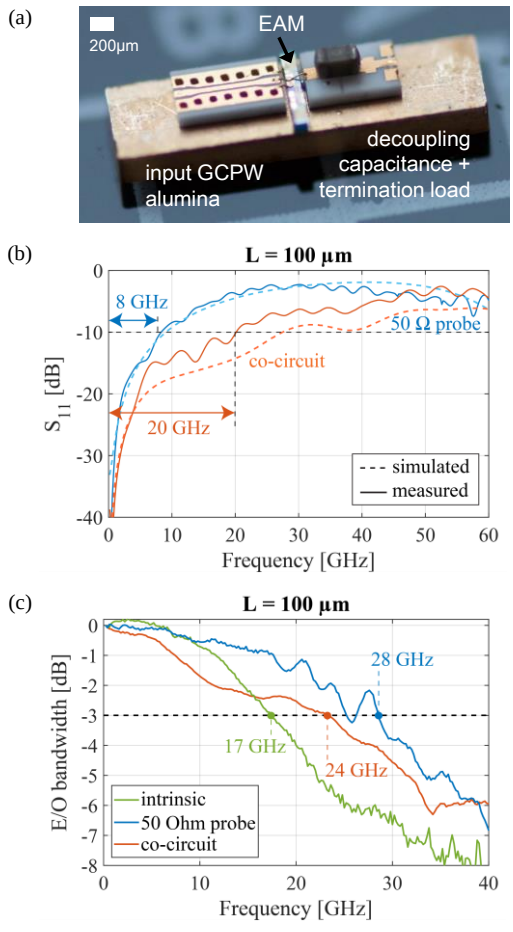

Fig. 10. (a) Fabricated EAM wire-bonded with the EAM submount. (b) Measured and simulated reflection parameter (S_{11}) of 100 µm-long EAM in two configurations: 50 Ω parallel load inside the RF probe and the EAM submount design. (c) E/O bandwidth of the intrinsic, 50 Ω parallel probe terminated and the EAM submount.

VI. Platform Association

The relative success of our approach in terms of platform integration is seen in the advantage of using the existing epitaxial layer stack, using the maximum of the platform offerings. We obtain the increase in speed by a factor of 3 compared to the currently offered Mach-Zehnder modulators [12]. The integration of a new building block does not have any impact on the performance of other building blocks and its integration with both actives and passives is demonstrated in this and previous work. Such a modulator structure is ready for use in transmitter integrated circuits, where high speed operation is needed.

With the example of the transmitter device, one can make a trade-off between the EAM length, its capacitance, the static extinction ratio, and the 3-dB bandwidth in conjunction with the DC bias and drive voltage and the source impedance. Out of these, two most important parameters can be chosen: the extinction ratio and the bandwidth. Fig. 11 shows the measured values for the two parameters (dots) depending on the modulator length. The results are presented for 40 nm detuning wavelength. A clear trade-off between the two is observed. The line for the static ER is its linear fit versus the EAM length, and the dashed line corresponds to the measured load-free 3-dB

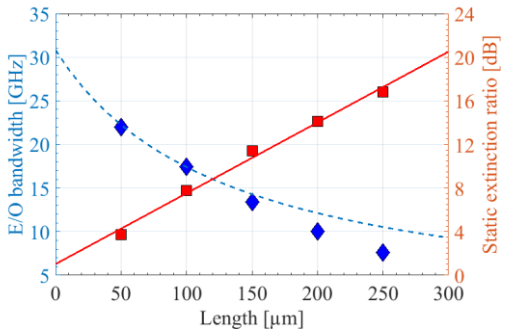

Fig. 11. The trade-off between the static extinction ratio and the intrinsic (load-free) EAM bandwidth at 40 nm detuning.

EAM bandwidth. On n-substrate the access pad alone will limit the bandwidth to around 30 GHz.

To achieve a static extinction ratio as high as 20 dB, a 200 µm-long EAM is needed and the resulting intrinsic (load-free) bandwidth is 8 GHz (17 GHz with 50 Ω parallel load), Shorter modulators of 50 µm provide 22 GHz bandwidth (45 GHz with 50 Ω parallel load), but only 4 dB static ER. In order to get the best out of the two, a separate EAM layer stack is feasible. It is technologically challenging to use a separate EAM layer stack, as it may require an additional regrowth step. If the EAM resistance and junction capacitance of such an optimized stack are kept the same, the RF-response would remain unchanged and the extinction ratio would improve.

VII. Conclusion

This paper introduces a new building block, an electro-absorption modulator, inside a foundry platform for photonic integrated circuits, focusing on platform speed increase. The electro-absorption modulator is now a part of the building block library, and can be used by external parties. An optimization framework for designing high speed electro-absorption modulators is proposed. We demonstrate 18 dB static extinction ratio, semi-cooled operation tested up to 60ºC and zero or negative chirp parameter for the optimal DC bias voltage. For a properly chosen detuning wavelength and temperature, a bias voltage of -0.75 V is achieved, compared to -2.3 V at room temperature. The intrinsic 3-dB bandwidth of the shortest reported modulator (50 µm) is 22 GHz, and with 50 Ω parallel termination it exhibits 45 GHz bandwidth. In order to improve the reflection parameter, we have designed an EAM submount keeping the return losses lower than -10 dB up to 20 GHz, an improvement by a factor of 2.5 compared to the on-chip measurement. The E/O bandwidth in this case is 24 GHz. By making the electrical co-design we improve the speed of the open access photonic integration platform. The increase in speed is observed through the available intrinsic bandwidth, and is improved from 9 GHz, previously offered by the platform, to 24 GHz demonstrated in this work.

Acknowledgment

The authors would like to thank Jean-Guy Provost for all the help in the laboratory with the measurement setups, and Karim Mekhazni for making the assembly. The devices in this work were fabricated by SMART Photonics through the JePPIX.eu MPW service.

References

[1] F. Kish, V. Lal, P. Evans, et al., "System-on-Chip Photonic Integrated Circuits," *Journal of Selected Topics in Quantum Electronics*, vol. 24, no. 1, pp. 1-20, 2018.

[2] H. Mardoyan, F. Jorge, O. Ozolins, et al., "204-GBaud On-Off Keying Transmitter for Inter-Data Center Communications," in *Optical Fiber Communication Conference Postdeadline Papers*, San Diego, 2018. paper Th4A.4.

[3] L. Chuang, L. Daris, P. Abolghasem, et al., "Demonstration of Fully Integrated 6λ x 200 Gbps (1.2 Tbps) PICs and Transceivers in L-band," in *European Conference on Optical Communication*, Rome, IT, 2018.

[4] M. Lauermann, R. Going, R. Maher, et al., "Multi-Channel, Widely-Tunable Coherent Transmitter and Receiver PICs Operating at 88Gbaud/16-QAM," in *2017 Optical Fiber Communications Conference and Exhibition (OFC)*, Los Angeles, 2017. pp. 1-3.

[5] M. Baier, F. M. Soares, Z. Zheng, et al., "112 Gb/s PDM-PAM4 Generation and 80 km Transmission Using a Novel Monolithically Integrated Dual-Polarization Electro-Absorption Modulator InP PIC," in *2017 European Conference on Optical Communication (ECOC)*, Gothenburg, Sweden, 2017. pp. 1-3.

[6] M. Theurer, M. Moehrle, U. Troppenz, et al., "4x56 Gb/s High Output Power Electroabsorption Modulated Laser Array With up to 7km Fiber Transmission in L-band," *Journal of Lightwave Technology*, vol. 36, no. 2, pp. 181-186, 2018.

[7] W. Yao, M. K. Smit and M. J. Wale, "Monolithic 300 Gb/s Parallel Transmitter in InP-Based Generic Photonic Integration Technology," *Journal of Selected Topics in Quantum Electronics*, vol. 24, no. 1, pp. 1-11, 2018.

[8] H. Debregeas, J. Decobert, N. Lagay, et al., "Selective-area-growth technology for flexible active building blocks," in *Advanced Photonics Congress*, Colorado Springs, CO, 2012. paper IM2A.3

[9] Yi-Jen Chiu, Hsu-Feng Chou, V. Kaman, et al., "High Extinction Ratio And Saturation Power Traveling-Wave Electroabsorption Modulator," *IEEE Photonics Technology Letters*, vol. 14, no. 6, pp. 792-794, 2002.

[10] W. Kobayashi, T. Yamanaka, M. Arai, et al., "Wide Temperature Range Operation of a 1.55-µm 40-Gb/s Electroabsorption Modulator Integrated DFB Laser for Very Short-Reach Applications," *IEEE Photonics Technology Letters*, vol. 21, no. 18, pp. 1317-1319, 2009.

[11] M. Smit, X. Leijtens, H. Ambrosius, et al, "An introduction to InP-based generic integration technology," *Journal of Semiconductor Science and Technology*, vol. 29, no. 8, pp. 1-41, 2014.

[12] L. M. Augustin, R.M. Lemos Alvares Dos Santos, E. den Haan, et al., "InP-Based Generic Foundry Platform for Photonic Integrated Circuits," *Journal of Selected Topics in Quantum Electronics*, vol. 24, no. 1, pp. 1-10, 2018.

[13] "Joint European Platform for Photonic Integration of Components and Circuits," [Online]. Available: http://www.jeppix.eu/, 2019

[14] M. Trajkovic, S. Latkowski, H. Debregeas, et al., "Monolithically integrated widely tunable laser and electro-absorption modulator in a generic InP integration platform," in *Proceedings of the 21st Annual Symposium of the IEEE Photonics Society Benelux Chapter*, Gent, Belgium, 2016.

[15] M. Trajkovic, F. Blache, K. Mekhazni, et al., "Impedance matching for high-speed InP integrated electro-absorption modulators," in *2018 IEEE Photonics Conference (IPC)*, Reston, VA, 2018. pp. 1-2.

[16] M. Trajkovic, F. Blache, F. Jorge, et al., "64Gb/s Electro Absorption Modulator Operation in InP-based Active-Passive Generic Integration Platform," in *2018 European Conference on Optical Communication (ECOC)*, Rome, Italy, 2018. pp. 1-3.

[17] J. Provost and F. Grillot, "Measuring the Chirp and the Linewidth Enhancement Factor of Optoelectronic Devices with a Mach–Zehnder Interferometer," *IEEE Photonics Journal*, vol. 3, no. 3, pp. 476-488, 2011.

[18] M. C. A. M. Koolen, "On Wafer High-Frequency Device Characterization," *Microelectronic Engineering*, vol. 19, no. 4, pp. 679-686, 1992.

[19] "Advanced Design System (ADS)," [Online]. Available: https://www.keysight.com/en/pc-1297113/advanced-design-system-ads, 2019.

Marija Trajkovic (S'16-M'19) received her B.S. and M.S. degree in Electrical Engineering from the University of Belgrade, Belgrade, Serbia. She did the experimental part of the Master Thesis at University of Southampton in Optical Research Centre. At the moment, she is a Ph.D. candidate on a joint programme between the Eindhoven University of Technology, Eindhoven, the Netherlands and III-V Lab, Palaiseau, France, working on the design and implementation of integrated high speed WDM transmitters.

Fabrice Blache received his Ph.D. degree in electronics from the University of Limoges, Limoges, France, in 1995. He is currently a Research Engineer with

III-V Lab, Palaiseau, France, a joint laboratory of Nokia Bell Labs, Thales Research and Technology and CEA-Leti. His main expertise is in the field of high frequency designs for optoelectronic modules. He is currently leading research activities for 100 Gb/s applications.

Hélène Debrégeas received the Engineering degree from Télècom Sud Paris, Evry, France, in 1994, and the aggregation of Mathematics in 1995. She received her Ph.D. degree working on widely tuneable lasers in 2007. She joined Alcatel Research Centre (now Nokia Bell Labs), Palaiseau, France, in 1997. She has been working on integrated InP transmitters based on electro-absorption modulated lasers and widely tuneable lasers. She spent two years in Nokia Bell Labs, US working on hybrid integration of InP and passive lightwave circuits. In 2018 she moved to Almae Technologies, Marcoussis, France. She contributed to more than 50 peer-reviewed journal and conference papers, patent applications, and a book chapter on "Widely Tuneable Lasers".

Kevin Williams received the B.Eng. degree in electronic engineering from the University of Sheffield, Sheffield, U.K., and the Ph.D. degree in physics from the University of Bath, Bath, U.K., in 1995. His research interests include the area of integrated photonic circuits. He is the Chair of the Photonic Integration research group at Eindhoven University of Technology, Eindhoven, The Netherlands. He was awarded a Royal Society University research fellowship at the University of Bristol, Bristol, U.K, in 1996. He moved to the University of Cambridge, Cambridge, U.K., in 2001 and was elected a Fellow at Churchill College. In 2006, he was awarded a European Commission Marie Curie Chair at the Eindhoven University of Technology, The Netherlands. In 2011, he received the Vici Award from the Netherlands Organization for Scientific Research (NWO).

Xaveer Leijtens (M'00–SM'13) studied physics at the University of Amsterdam where he received the M.Sc and PhD degree in high energy physics. In 1993, he joined the photonic integrated circuits group at TU Delft. In 2000 he moved to TU Eindhoven where he is associate professor in the photonic integration group. His interest focuses on photonic IC design and measurement automation. He is leading the design effort within the Joint European InP platform, JePPIX.eu. He has been a member and chairman of the board of the IEEE Photonics Society Benelux chapter. He was an Associate Editor of IEEE Photonics Technology Letters (2007–2011). He (co)authored more than 350 scientific papers and conference contributions.